Journal of Cleaner Production 297 (2021) 126498

Contents lists available at ScienceDirect

Journal of Cleaner Production

journal homepage: www.elsevier.com/locate/jclepro

Difference in performance and mechanism for methylene blue when TiO_2 nanoparticles are converted to nanotubes

Lin Niu [a], Xiaoli Zhao [a, *], Zhi Tang [a], Hongzhou Lv [a], Fengchang Wu [a], Xiaolei Wang [a], Tianhui Zhao [a], Junyu Wang [a], Aiming Wu [a], John.P. Giesy [b]

[a] State Key Laboratory of Environmental Criteria and Risk Assessment, Chinese Research Academy of Environmental Sciences, Beijing, 100012, China
[b] Toxicology Centre, University of Saskatchewan, Saskatoon, Saskatchewan, Canada

ARTICLE INFO

Article history:
Received 24 September 2020
Received in revised form
12 February 2021
Accepted 21 February 2021
Available online 25 February 2021

Handling editor: M.T. Moreira

Keywords:
TiO_2 nanotubes
TiO_2 nanoparticles
Adsorption
Photocatalysis
Organic pollutants

ABSTRACT

There are few reports on the diversification in adsorption and photo-catalysis caused by morphological changes. In this study, TiO_2 nanotubes (TiO_2 NTs) were synthesized by alkaline hydro-thermal method using commercial TiO_2 nanoparticles (TiO_2 NPs) as raw materials. When TiO_2 nanoparticles are converted to nanotubes, the difference in adsorption and photocatalytic performance was analyzed using methylene blue (MB) as a model pollutant. The results showed that TiO_2 NPs exhibited low adsorption capacity and greater photocatalytic activity for MB. In contrast, TiO_2 NTs showed dual functions of adsorption and photo-catalysis. It exhibited better adsorption performance for MB and the maximum uptake was 102.41 mg/g. However, the photo-catalytic activity changed because the hydro-thermal method altered the crystal structure and increased the gap energy of TiO_2 NTs, which led to the partial reduction of photo-catalytic activity compared to TiO_2 NPs. The dominating free radicals were $\cdot OH$, followed by $\cdot O_2^-$ in the process of MB photodegradation by TiO_2 NPs while $\cdot OH$ and $\cdot O_2^-$ were main radicals in the process of MB photodegradation by TiO_2 NTs. Moreover, 99% MB was degraded in 24 min via adsorption and photo-catalysis synergy under the following optimal conditions: TiO_2 NTs dose = 6 mg, pH = 9, and light intensity = 19 A. Compared with other photo-catalysts reported, TiO_2 NTs exhibited a superior performance through adsorption and photo-catalysis synergy with advantages of faster degradation, less catalyst dose and high efficiency. This work hopes to provide reference for the design and synthesis of materials with dual functions of adsorption and photo-catalysis.

1. Introduction

For the past few years, the combination of adsorption with photo-catalysis has been reported to effectively remove organic pollutants (Chen et al., 2020a; Yu et al., 2021; Zhu et al., 2020; He et al., 2020). Pollutants can be attached to a material through adsorption, and are then degraded through the photo-catalytic process, which not only solves the problem of adsorption saturation, but also solves the difficulty of recycling of photo-catalysis (Sheng et al., 2019). The basis of adsorption-photo-catalysis technology is a material; moreover, the method of constructing an adsorption-catalytic dual-functional material is the key to improve efficiency of removal of contaminants (Chen et al., 2020b).

TiO_2 is not only widely used in photo-catalytic processes because of its stability, non-toxicity, and low cost but also because it is one of the most commercially promising photo-catalytic materials (Ye et al., 2020). Currently, there are increasing concerns related to TiO_2-based materials with dual functions of adsorption and photo catalysis (Gu et al., 2019; Huang et al., 2019; Bian et al., 2021; Qiu et al., 2020; Zheng et al., 2021). The commonalities of these materials are: 1) they are all composite materials, and the adsorption-photocatalysis synergy were achieved by use of the photocatalytic activity of TiO_2 and the adsorption performance of other materials; 2) the drawbacks associated with them such as complex preparation conditions, energy-consuming preparation, and presence of metallic components limit their large-scale industrial applications. In the context of this technology, there is an urgent need for single materials that are easy to prepare in large quantities with minimal use of toxic substances, that are efficient to use and recover to be used again.

* Corresponding author.
E-mail addresses: zhaoxiaoli_zxl@126.com (X. Zhao), wufengchang@vip.skleg.cn (F. Wu).

https://doi.org/10.1016/j.jclepro.2021.126498
0959-6526/

Compared with TiO_2 nanoparticles (NPs), the morphology and specific surface area of TiO_2 (NTs) are easier to control and the stability of TiO_2 NPs is better, so the dual functions of adsorption-photo-catalysis are easier to achieve in the case of TiO_2 NTs than in the case of TiO_2 NPs. Mostly TiO_2 NTs are synthesized using commercially TiO_2 NPs by many researchers (Cheng et al., 2019; Fang et al., 2019; Pang and Abdullah, 2012). They focus on the preparation of TiO_2 NTs and explored the influence of various factors on their morphology and structure. For instance, Sandoval et al. (2017) synthesized TiO_2 NTs and explored effects of different sodium content on the removal of methylene blue by combined adsorption and photocatalysis. Jiang et al. (2012) evaluated the effect of calcination temperature on the adsorption and photocatalytic activity of hydrothermally synthesized TiO_2 NTs. Zulfiqar et al. (2020) found that organic solvent played an important role on the adsorption and photocatalytic performance of TiO_2 nanotubes. However, few studies have linked TiO_2 NTs with TiO_2 nanoparticles precursor to explore the changes in adsorption and photo-catalysis performance when their morphologies are changed.

In this study, the adsorption and photo-catalysis performance and mechanism of TiO_2 NPs and NTs were investigated. To facilitate the investigation of the mechanisms, TiO_2 NPs were simply transformed via an alkaline hydro-thermal method at certain closed pressure, which altered the morphology and properties of the material (i.e., TiO_2 NPs). Morphologies and properties of obtained TiO_2 NTs were characterized by transmission electron microscopy (TEM), X-ray photoelectron spectroscopy (XPS), Fourier transform infrared (FTIR) spectroscopy, and the Brunauer–Emmett–Teller (BET) method. The performance difference between TiO_2 NPs and TiO_2 NTs was investigated through adsorption and photo-catalysis experiments using methylene blue (MB) as a target pollutant. This study revealed the influence of changes in morphology and crystalline form on the adsorption and photo-catalysis performance of TiO_2 through comparative studies, and provided a reference for the development and design of materials with high adsorption and high photo-catalysis performance.

2. Materials and methods

2.1. Materials

TiO_2 NPs were purchased from J&K Scientific Ltd. (25–50 nm, average surface area 19.6 m^2/g). MB was purchased from Sigma-Aldrich and was used as a target pollutant. NaOH and HCl were purchased from Macklin Biochemical Technology Co., Ltd. All chemicals and reagents used in this study were of analytical grade or relatively greater purity. The water (ultrapure water, 18.2 MΩ cm) used in all experiments was prepared using a Milli-QSP reagent water system (Millipore, Bedford, MA).

2.2. Preparation of protonated TiO_2 NTs

TiO_2 NTs were prepared via the alkaline hydro-thermal method (Zhao et al., 2019). First, 3 g of anatase-phase TiO_2 NPs powder was dispersed in 100 mL of a 10 M NaOH solution and vigorously stirred for 24 h. Subsequently, the mixture was autoclaved at 150 °C for 24 h. The obtained white product was washed with DI water until the supernatant pH became neutral and then soaked in a 0.5 M hydrochloric solution for 5 h. Interlayer sodium ions were anticipated to be exchanged for protons during the soaking of the nanotubes in the acidic solution. Afterward, the protonated TiO_2 NTs were again washed to pH 7 with DI water. Finally, the products were dried at 90 °C.

2.3. Characterization

TEM images were evaluated using FEI Tecnai G2 F20 field-emission transmission electron microscope (USA) operating at 200 kV. The surface composition of TiO_2 NTs and TiO_2 NPs was determined by XPS (ESCALAB 250Xi, Thermo Scientific, UK). To verify the chemical composition of the samples (TiO_2 NTs and TiO_2 NPs before and after adsorbed or catalyzed MB), FTIR spectroscopy was conducted using a Thermo Fisher Nicolet IS5 infrared spectrometer (USA) in the wavelength range of 400 cm^{-1} to 4000 cm^{-1} at a resolution of 4 cm^{-1}; moreover, 64 scans were recorded for the background and samples. The BET surface area was measured by nitrogen adsorption at −196.15 °C and nitrogen desorption at 200 °C for 12 h. UV–visible diffuse reflectance spectroscopy (DRS) was performed using UV spectrophotometer (UV2700, Shimadzu, Japan). Photo-luminescence (PL) spectra of TiO_2 NTs or TiO_2 NPs were collected using by an Edinburgh FLSP 920 fluorescence spectrometer equipped with a 900 W xenon lamp; moreover, these PL spectra were collected in the wavelength ranger of 400–700 nm at a step size of 0.5 nm and a temperature of 27.40 °C.

2.4. Photo-electrochemical measurements

Photo-electrochemical measurements were performed using a photoelectric catalytic testing system (CHI760E) with a three-electrode system, which consisted of a working electrode, counter electrode, and reference electrode. Samples of TiO_2 NPs and TiO_2 NTs, coated on indium tin oxide (ITO) glass were used as working electrodes. A platinum electrode and silver chloride electrode were used as the counter electrode and reference electrode, respectively. A 0.5 M Na_2SO_4 aqueous solution worked as the electrolyte. Electrochemical impedance spectroscopy (EIS) was performed and its frequency ranged from 100 kHz to 1 Hz with an amplitude of the sinusoidal wave of 5 V. Additionally, to separate photo-generated electron–hole pairs, the photocurrent experiment was conducted under the same conditions as those used during the EIS experiment. The initial voltage was changed to 0.248 V. A UV light source (i.e., a 300 W xenon lamp with a visible light cut–off of $\lambda > 420$ nm) was located at a distance of 15 cm from the photo-electrochemical cell.

2.5. Experiments

2.5.1. Conditional optimization of TiO_2 NTs under simultaneous photo-catalysis–adsorption experiment

A simultaneous photo-catalysis–adsorption experiment was conducted to optimize conditions and assess efficiencies of removal of pollutants from actual sewage treatment plants. The simultaneous photo-catalysis–adsorption system was employed under a 300 W xenon lamp (with a visible light cut–off of $\lambda > 420$ nm) placed at a distance of 15 cm. According to the single variable method, while maintaining the concentration of MB at 10 mg/L, one of the following factors was changed to measure the removal efficiency of MB: TiO_2 NT dosage (4, 6, and 8 mg), initial pH (3–11), and current intensity (15, 17, and 19 A (A)). Typically, during irradiation, 3 mL of the sample was withdrawn at specific time intervals and immediately centrifuged; subsequently, the resultant supernatant was analyzed at a wavelength of 665 nm by a UV–vis light spectrophotometer.

To evaluate stabilities of TiO_2 NTs, four reusability experiments were conducted. After the adsorption and photo-degradation of MB by TiO_2 NTs under optimum conditions, TiO_2 NTs were collected and washed with ultrapure water; subsequently, the washed TiO_2 NTs were dried at 65 °C. Finally, dried TiO_2 NTs were reused under

the same conditions.

2.5.2. Evaluation of adsorption and catalysis performance of TiO_2 NTs and TiO_2 NPs via dark adsorption and photo-catalysis experiment

MB was used as a probe dye to evaluate the adsorption and catalysis capabilities of TiO_2 NPs or TiO_2 NTs. An adsorption experiment was implemented under dark conditions. Typically, in this experiment, TiO_2 NPs or TiO_2 NTs (6 mg) were dispersed into 10 mg/L of MB aqueous solutions with pH values of 9 (adjusted by 0.1 mol/L NaOH or HCl solution). Afterward, 3 mL of the sample was taken at given intervals and immediately centrifuged to discard the sediment. Subsequently, the resultant supernatant was analyzed by a UV−vis light spectrophotometer.

A photo-catalysis experiment was carried out under a 300 W xenon lamp (with a visible light cut−off of $\lambda > 420$ nm) located at a distance of 15 cm. The photocurrent was 19 A, which represented the light intensity in this experiment. Before the photocatalytic experiment, conditions for the dark adsorption experiment were the same as those for the adsorption experiment and the solution was magnetically stirred for 30 min to reach adsorption−desorption equilibrium and then turning on the light to carry out photocatalytic experiment. The sample was removed within a given period and measured at 665 nm by UV−vis light Spectrophotometer.

Furthermore, in order to determine the main active species in TiO_2 NPs or TiO_2 NTs, radical−trapping experiments were conducted under the light. Glycerol, p−benzoquinone (BQ), and ethylenediaminetetraacetic acid tetrasodium salt (EDTA-2Na) were used as scavengers of hydroxyl radicals ($\cdot OH$), superoxide radicals ($\cdot O_2^-$), and holes (h^+), respectively.

3. Results and discussion

3.1. Characterizations

3.1.1. Transmission electron microscopy (TEM)

In the process of transformation of TiO_2 NPs to TiO_2 NTs, the sheet folding mechanism was assumed (By Tomoko Kasuga et al., 1999; Wang G Q H et al., 2002; Sun and Li, 2003). As shown in Fig. 1, firstly, the three-dimensional TiO_2 NPs was transformed to two-dimensional (2D) lamellar products with a mass of Ti−O−Na bonds after alkali treatment. Then the product was washed by water and hydrochloric solution to form new Ti−O−H bonds instead of old Ti−O−Na bonds. Finally, the tubular structure was formed by bending and rolling further of sheet due to residual electrostatic repulsion of Ti−O−Na bonds. Morphologies and microstructures of TiO_2 NTs and TiO_2 NPs prior to and after adsorption and photo-catalysis of MB were.

Observed by TEM; the corresponding morphologies and microstructures are shown through TEM images (Fig. 2). The diameter of TiO_2 NPs is in the range of 25−50 nm (Fig. 2a). The measured lattice distance of 0.24 nm, which possibly corresponds to the (021) plane of anatase TiO_2 is shown (Fig. 2b). This plane is not observed in the TEM image of TiO_2 NTs (Fig. 2d) (Pang and Abdullah, 2012). In addition, TiO_2 NTs exhibit irregular arrangement. Besides, the TiO_2 NTs possess hollow and uniform tubular structures, outer and inner diameters of which are in the range of 8−9 nm and 5−6 nm, respectively (Fig. 2c and d). These TEM results indicate that TiO_2 was successfully transformed from nanoparticles to nanotubes. Fig. 2(e, g) and 2(f, h) will be discussed in sections 3.3.2 and 3.4.1, respectively.

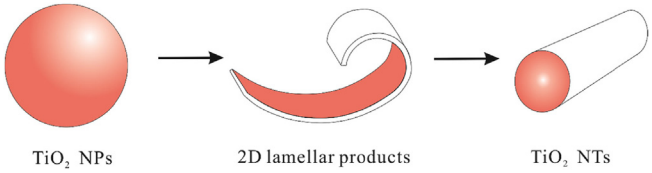

Fig. 1. The transformation diagram from TiO_2 NPs to TiO_2 NTs.

3.1.2. XPS

The wide difference between TiO_2 NPs and TiO_2 NTs was identified via XPS (Fig. 2i). The full XPS spectrum of TiO_2 NTs was compared with that of TiO_2 NPs. It was found that the typical four peaks of Ti3p, C1s, O1s, and Ti2p in the spectra of TiO_2 NTs were consistent with those of TiO_2 NPs. The XRD analysis results obtained in our previous study (Zhao et al., 2019) have shown that the crystal forms of TiO_2 NTs are inconsistent with those of TiO_2 NPs. Moreover, the typical anatase phase is found in TiO_2 NPs, and sodium hexatite is the primary phase in TiO_2 NTs (Zhao et al., 2019). A possible reason is that dissolution of TiO_2 NPs breaks the Ti−O−Ti bonds and generates free Ti ions to react with NaOH, forming $Na_2Ti_6O_{13}$ (Zhao et al., 2019); this leads to a change in the crystal structure of TiO_2. In this study, compared with TiO_2 NPs, the XPS spectrum of TiO_2 NTs exhibited two novel peaks at the binding energy positions of 495.0 eV and 1070.0 eV for TiC $2p_{3/2}$ and Na (Fig. 2i), respectively, which can be ascribed to the formation of Ti−C bonds and the retention of Na element caused by the preparation of TiO_2 NTs via the alkaline hydrothermal method.

To further understand the chemical states of Ti2p, C 1s, O 1s, the high−resolution XPS spectra of TiO_2 NPs and TiO_2 NTs (Figure S1(a−c) and S2(a−c)) were analyzed. Binding energies of Ti in case of TiO_2 NTs (458.4, 464.2 eV) and TiO_2 NPs (458.5, 464.2 eV) were assigned to $2p_{3/2}$ and $3p_{1/2}$, respectively, revealing the existence of Ti in the form of Ti^{4+} (Wang et al., 2009, 2018, 2020). The Ti 2p intensity of TiO_2 NTs was apparently greater than that of TiO_2 NPs, which indicated the presence of relatively more Ti^{4+} in TiO_2 NTs. Moreover, $Ti2p_{3/2}$ of TiO_2 NTs was shifted by approximately 0.11eV compared to that of TiO_2 NPs, which manifests that the electron cloud density was enhanced. Further, the O1s spectrum was deconvoluted into three peaks. The peaks corresponding to the Ti−O bond was observed at 529.7 eV and 529.9 eV in the high−resolution O1s spectra of TiO_2 NPs and TiO_2 NTs, respectively (Chen et al., 2020c; Guo et al., 2020). The peak at 531.7 eV was attributed to the −OH, while the peak at 532 eV was ascribed to the surface adsorbed hydroxyl.

Groups in the TiO_2 NPs (Hou et al., 2019; Santhi et al., 2020). Besides, the peak at 530.5 eV was ascribed to Ti_2O_3 in TiO_2 NTs (Alves et al., 2017). The mechanism of MB adsorbed on TiO_2 surface and the stability of TiO_2 after MB photo-catalysis will be discussed in section 3.3.2 and 3.4.1, respectively.

3.1.3. Fourier transform infrared (FTIR) spectroscopy

The molecular structure and chemical composition of TiO_2 NTs and TiO_2 NPs before and after the adsorption−photo-catalysis of MB were determined through FTIR spectroscopy; the FTIR spectroscopy results are displayed (Fig. 3a). The band extending from 400 to 700 cm^{-1} was attributed to the two characteristic peaks of stretching vibrations of Ti−O and Ti−O−Ti bonds (Zhao et al., 2019; Kadam et al., 2020; Yu et al., 2020; Gao et al., 2020; Zhou et al., 2019). The peak corresponding to the Ti−O bonds in TiO_2 NTs was shifted to a relatively low wavelength and a peak was absent in the FTIR spectrum of TiO_2 NTs compared to that of TiO_2 NPs, which possibly indicated a change in the crystal structure of TiO_2. The absorption bands at approximately 1629 and 3319 cm^{-1} belonged to the stretching vibrations of −OH groups, which indicated the adsorption of H_2O, −OH groups on the surface of TiO_2 NTs (Li et al.,

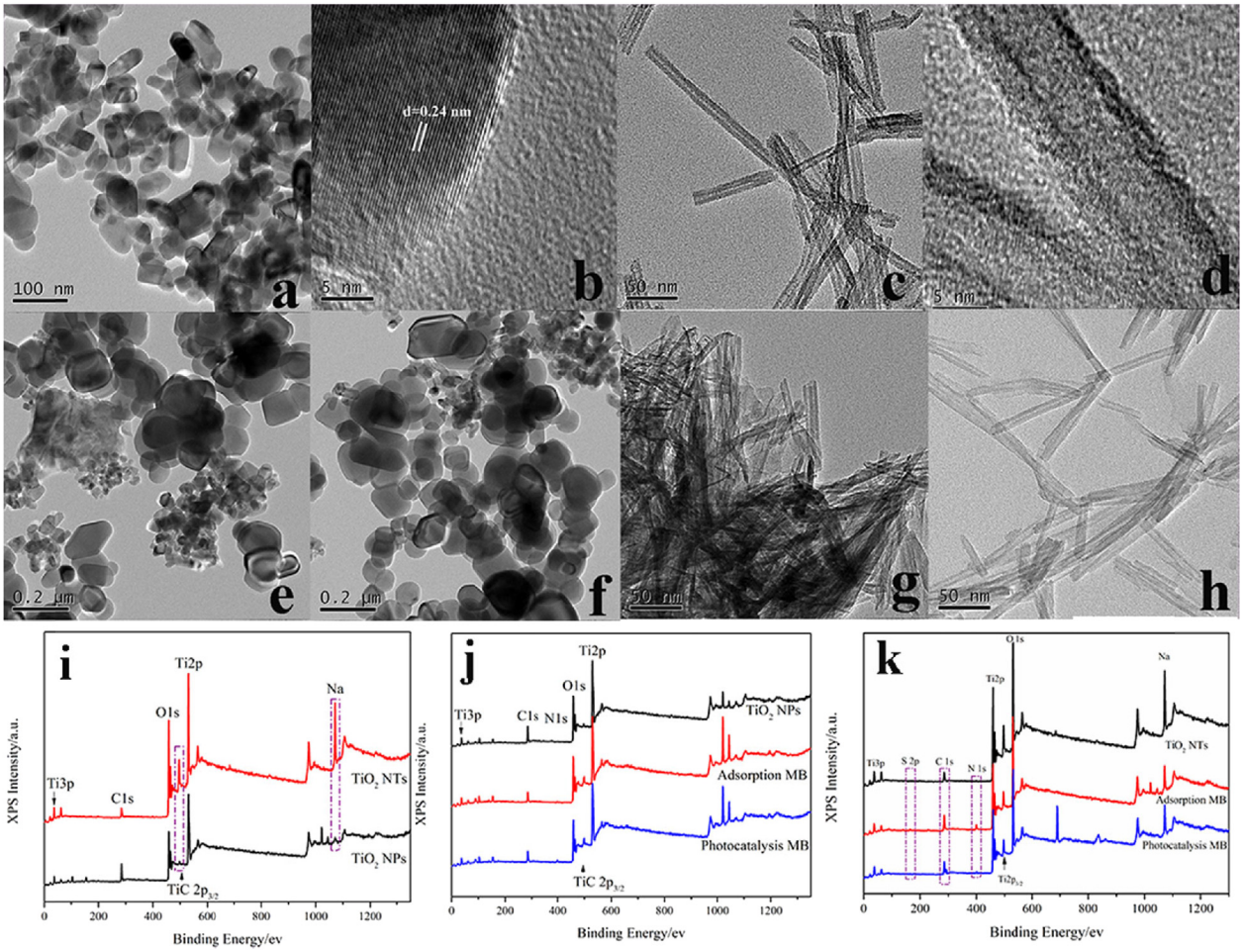

Fig. 2. TEM images of TiO_2 NPs(a,b), TiO_2 NTs (c,d), TiO_2 NPs(e) and TiO_2 NTs(g) after MB adsorption, TiO_2 NPs(f) and TiO_2 NTs(h) after MB photo-catalysis; Full XPS spectrum of TiO_2 NPs and TiO_2 NTs(i), TiO_2 NPs(j) and TiO_2 NTs(k) after adsorption and photo-catalysis MB, respectively.

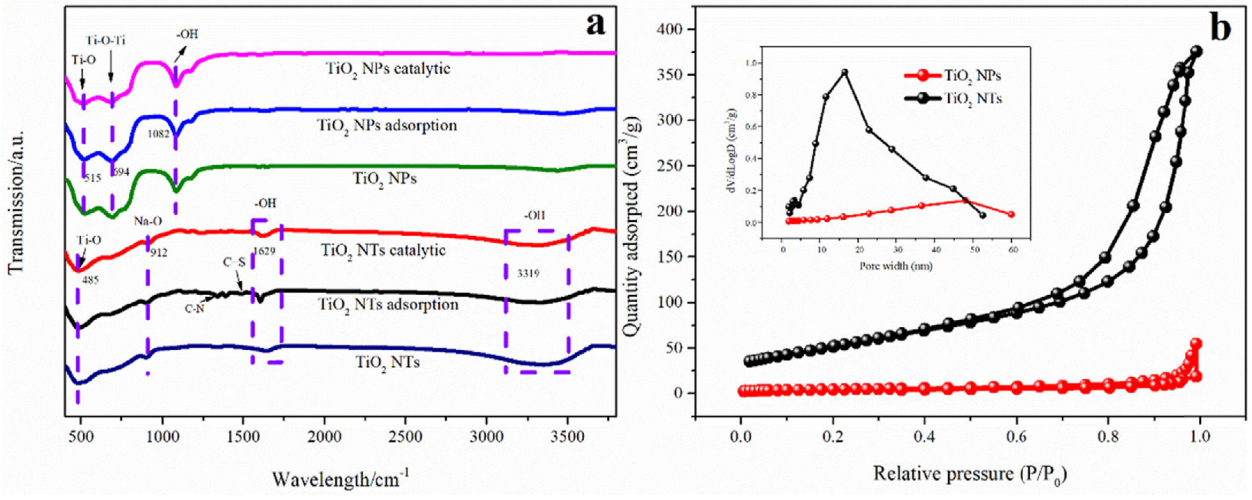

Fig. 3. FTIR spectrum of before and after adsorption and photo-catalysis MB by TiO_2 NPs, TiO_2 NTs, respectively(a), Nitrogen-desorption isotherms of TiO_2 NPs and TiO_2 NTs, and the inset is the distribution of pore diameter(b).

2020; Shao et al., 2015). A strong absorption peak at 912 cm^{-1} was attributed to the Na—O bonds, which were formed because of the preparation of TiO_2 NTs by the alkaline hydrothermal method. In the spectra of TiO_2 NPs, the peak at 1082 cm^{-1} was attributed to —OH vibrations (Seo et al., 2020).

3.1.4. Brunauer–Emmett–Teller (BET) method

The N_2 adsorption–desorption isotherms and Barrett–Joyner–Halenda (BJH) pore-size distribution plots are shown (Fig. 3b). Based on International Union of Pure and Applied Chemistry (IUPAC) classification, isotherms of TiO_2 NTs and TiO_2 NPs were in accordance with their classification as type IV, which indicated that TiO_2 NTs and TiO_2 NPs had mesoporous structures. At lower relative pressures, monolayer adsorption was observed in the case of both TiO_2 NTs and TiO_2 NPs. Hysteresis loops of TiO_2 NPs and TiO_2 NTs appeared at relatively higher pressure, which indicated that capillary agglomeration occurred in mesopores (Al-Hajji et al., 2020). Nevertheless, the shape of the hysteresis loop of TiO_2 NPs was narrower than that of TiO_2 NTs, which suggested that the percentage of mesopores present in the structure of TiO_2 NPs was less than that present in the structure of TiO_2 NTs. The mesopore diameter of TiO_2 NTs was in the range of 15–17 nm (Fig. 3b inset). The pore volume of TiO_2 NTs was 0.58 cm^3/g. The surface area (191.56 m^2/g) of TiO_2 NTs was 12.66 times the surface area of TiO_2 NPs (15.13 m^2/g). Further, mean pore diameter of TiO_2 NTs (10.95 nm) was less than that of TiO_2 NPs (21.43 nm). Consequently, the difference in surface areas between TiO_2 NTs and TiO_2 NPs was attributed to mesoporous walls and tube openings of TiO_2 NTs (Liu et al., 2020), which might be the reason to improve the adsorption capability of TiO_2 NTs.

3.2. Conditional optimization

The simultaneous photo-catalysis–adsorption experiment was employed by turning.

On the UV light while adding titanium dioxide. To study adsorption–catalysis synergistic effect of TiO_2 NTs, the concentration of the target pollutant (MB) was maintained at 10 mg/L; moreover, one of the following factors was simultaneously changed: TiO_2 NTs dose, pH, and photocurrent intensity. In addition, other conditions remained unchanged. The absorbance after the adsorption and catalysis of MB was measured, and the role of different factors in the adsorption–catalytic degradation of MB by TiO_2 NTs was investigated.

3.2.1. Amounts of TiO_2 NTs

The amount of TiO_2 NTs has a considerable effect on the removal efficiency; therefore, the effect of different dose of TiO_2 NTs (4, 6, and 8 mg) was investigated. A higher removal rate was obtained with an increase in the amount of TiO_2 NTs (Fig. 4a). On the one hand, the characterization of N_2 adsorption–desorption isotherms showed that TiO_2 NTs had mesoporous structures. The mesoporous structure of TiO_2 NTs may provide adsorption sites, which promoted the adsorption of MB. Alternatively, according to the XPS characterization of TiO_2 NTs, it found the retention of Na element. Due to cation exchange, Na titanate nanotubes promote adsorption of MB (Sandoval et al., 2017), in order that MB is adsorbed relatively more easily on the surface of TiO_2 NTs. When the degradation time was 20 min, almost the same proportion of MB was adsorbed regardless of whether the dose was 6 or 8 mg. To reduce industrial costs and save resources, a 6 mg dose of TiO_2 NTs was used in further experiments.

3.2.2. pH values

The MB removal efficiency of TiO_2 NTs at pH values in the range of 3–11 was determined. The results presented in Fig. 4b indicate that as the pH increases, the removal rate increases. This might be related to the isoelectric point of TiO_2 NTs. When the pH of the solution is higher than the isoelectric point of TiO_2 NTs (point of zero charge (PZC) = 3.2), a negative charge exists on the surface of TiO_2 NTs. The higher the pH, the stronger the electrostatic adsorption and thus more the amount of MB adsorbed. Further, more the amount of MB adsorbed, the higher the removal efficiency. When pH = 9, the removal rate is the highest; therefore, pH 9 is the optimal pH.

3.2.3. Photo-current intensity

Photo-current intensity is one of the important factors which affects photo-catalysis. Efficiency of removal of MB by TiO_2 NTs under different photo-current intensities was investigated (Fig. 4c). Efficiency of removal was directly proportional to intensity of light. This is because the greater intensity of photo-current generates easier electron transitions, which results in formation of relatively more electron–hole pairs; furthermore, the more electron–hole pairs, the better the catalytic performance. When the photo-current intensity was 19 A, the removal efficiency of MB was greatest; therefore, a photo-current intensity of 19 A was selected for subsequent experiments.

Based on the results of conditional optimization, optimal conditions were as follows: TiO_2 NT dose = 6 mg, pH = 9, and light intensity = 19 A. Notably, the removal efficiency of TiO_2 NTs was higher than the removal efficiencies of other catalysts (see Table 1). This result demonstrates that TiO_2 NTs have the advantages of low dose, high degradation efficiency and relatively short degradation time.

3.2.4. Reusability studies

Reusability is an important factor to verify the stability and recyclability of materials. In this study, four consecutive cycles were conducted using the same conditions. TiO_2 NTs retained 83.8% of adsorption–photo-catalysis activity, which indicated that its removal efficiency did not decrease significantly (Fig. S3). Thus, it was demonstrated that TiO_2 NTs with outstanding recyclability could be used repeatedly.

3.3. Adsorptive performance of TiO_2 NTs and TiO_2 NPs

3.3.1. Adsorption kinetics of TiO_2 NTs and TiO_2 NPs

Adsorption plays an important role in the removal organic pollutants. The adsorption performances of TiO_2 NTs and TiO_2 NPs are shown (Fig. 4d). For TiO_2 NTs, 33.89% of MB was quickly adsorbed within 2 min and the maximum adsorption capacity (qe) of 102.41 mg/g was reached in approximately 30 min TiO_2 NPs exhibited relatively low MB adsorption (1.6 mg/g) within 30 min.

To evaluate the rate of adsorption by TiO_2 NTs, kinetic models of pseudo–first–order and pseudo–second–order rates were determined (Equations (1) and (2)).

$$\log(q_e - q_t) = \log(q_e) - \left(\frac{k_1}{2.303}\right) \cdot t \tag{1}$$

$$\frac{t}{q_t} = \frac{1}{k_2 q_e^2} + \frac{1}{q_e} \cdot t \tag{2}$$

where: k_1 and k_2 are the rate constants of adsorption (min^{-1} and $g \cdot mg^{-1} min^{-1}$, respectively), q_t is the amount of MB adsorbed by TiO_2 NTs at a specific time ($mg \cdot g^{-1}$), q_e is equilibrium adsorption amount ($mg \cdot g^{-1}$).

Adsorption kinetics revealed that the coefficient of determination (R^2 up to 0.9941) of the pseudo-second-order kinetic model was greater than that of the pseudo-first- order kinetic model (R^2 up to 0.9638), which indicated that the computed and experimental values of q_e were almost consistent with each other (Fig. 4e–f). Thus, it can be easily inferred that the pseudo-second-order kinetic model is more appropriate to describe the

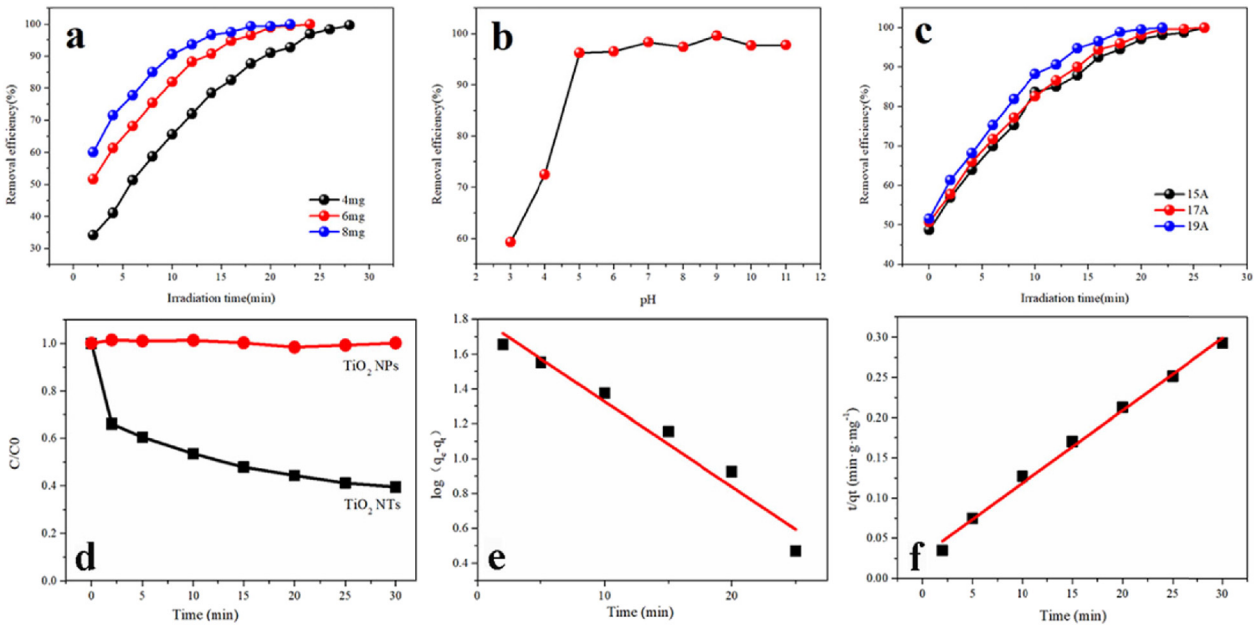

Fig. 4. Impact factors affecting removal efficiency including TiO_2 NTs dose (a), pH value (b), and photocurrent intensity (c); Adsorption performances of TiO_2 NPs and TiO_2 NTs (d); The pseudo-first-order kinetic curves (e) and pseudo-second-order kinetic curves (f) of TiO_2 NTs.

Table 1
Comparison of TiO_2 NTs with other photo-catalysts.

Materials	Photo-catalyst dose (mg)	Target pollutant: MB		Catalyst:MB (mg/mg)	Light source	Degradation time (min)	Removal efficiency (%)	Ref.
		Concentration (mg/L)	Volume (mL)					
TiO_2/rGO−8/500	160	10	200	80:1	UV	120	100	Kusiak-Nejman et al. (2019)
10 wt% WO_3/TiO_2	30	10	50	60:1	UV	180	99	El-Yazeed and Ahmed (2019)
TiO_2−MoS_2 (wt% = 5:7)	50	50	200	5:1	UV	40	80	Ibukun et al. (2019)
SnO_2 (600 °C)	10	10	100	10:1	UV	180	90.70	Sadeghzadeh-Attar (2018)
ZnO/$NiFe_2O_4$ NPs	75	16	50	375:4	UV	70	>95	Adeleke et al. (2018)
SnO_2 NPs (170 °C)	20	10	70	200:7	UV	30	100	Tammina et al. (2018)
TiCr10	100	3	100	625:2	UV	60	>90	Ahmed et al. (2017)
TiFe7	100	3	100	625:2	UV	60	>95	Ahmed et al. (2013)
DTC−5.0	10	8	100	25:1	UV	180	90	Nguyen-Phan and Shin (2011)
La (0.5%)−Eu (1.0%)/TiO_2 calcined 600 °C	200	40	50	100:1	UV	120	100	Shi et al. (2011)
NiO catalyst	100	10	100	100:1	UV	120	>45	Wan et al. (2013)
ZRGO80	200	10	200	100:1	UV	20	>90	Qin et al. (2017)
TiO_2−$HTaWO_6$ nanocomposite	20	20	100	10:1	UV	105	>85	Lin et al. (2012)
3 mol% $WO_3/ZnWO_4$	100	30	100	100:3	UV	480	55.54	Keereeta et al. (2015)
Cu@$CuSO_4/TiO_2$	20	5	150	80:3	UV	60	94	Zarghami et al. (2015)
ZnO 47.0 nm	20	10	200	10:1	UV	60	70	Mekasuwandumrong et al. (2010)
rGO−CdO	50	3	50	1000:1	UV	110	80	Kumar et al. (2016)
CdS/CNT−TiO_2 composite	10	3	50	200:3	UV	150	98.6	Zhu et al. (2012)
TiO_2 submicrosphere	250	20	500	25:1	UV	90	>95	Zhang et al. (2009)
Sm^{3+}−$BiPO_4$	125	10	250	50:1	UV	50	97	Nithya et al. (2019)
TiO_2 NTs	6	10	100	6:1	UV	24	99	This work

adsorption behavior of MB on TiO_2 NTs.

3.3.2. Mechanisms of adsorption of MB

The surface topography and elemental composition of TiO_2 NTs and TiO_2 NPs after the adsorption of MB as determined by TEM, XPS and FTIR spectroscopy.

After TiO_2 NTs and TiO_2 NPs adsorbed MB, the changes in their morphologies were different. The morphology of TiO_2 NPs did not change significantly after adsorption of MB, which suggested that TiO_2 NPs had poor adsorption capacity for MB (Fig. 2e). However, the disappearance of partial hollow structure indicated that the surface of TiO_2 NTs might have been occupied by MB (Fig. 2g). Thus, it can be speculated that TiO_2 NTs are possibly more attractive toward MB compared with TiO_2 NPs. There were no distinct differences in Ti3p, C1s, O1s and Ti2p peaks in the XPS spectra of TiO_2 NPs before and after MB adsorption (Fig. 2j and S1 (d−f), which

indicated that there was no interaction between TiO_2 NPs and MB, which was consistent with the experimental results. However, a completely different result was obtained in the case of TiO_2 NTs after MB adsorption. In the spectrum of the TiO_2 NTs after MB adsorption, S2p was observed at 164.0 eV; at the same time, intensities of C1s and N1s peaks were stronger compared with those of C1s and N1s peaks before adsorption of MB (Fig. 2k), which indicated that MB was successfully adsorbed onto TiO_2 NTs. Moreover, the peak corresponding to elemental Ti did not shift appreciably after adsorption of MB by TiO_2 NTs, but its intensity was significantly less, which indicates that MB adsorbed on surfaces of TiO_2 NTs might have hindered detection of Ti. Notably, the peak corresponding to the C=O bond disappeared. Intensities of the O1s spectrum (Ti−O (529.3 eV), Ti_2O_3(531.0 eV)) and C1s spectrum (C−C (284.8 eV), C−OH (287.7 eV)) decreased or increased, respectively (Figs. S2(d−f)). This can be attributed to transfer of electrons between TiO_2 NTs and MB, which indicates that chemical bonds play an important role in the adsorption of MB.

In the FTIR spectrum of TiO_2 NPs after MB adsorption (Fig. 3a), all TiO_2 NP samples remained almost unchanged. However, in the FTIR spectrum of TiO_2 NTs after MB adsorption (Fig. 3a), two new absorption peaks appeared at 1342 cm^{-1} and 1485 cm^{-1}, which were attributed to the stretching vibrations of C−N and C=S bonds in MB adsorbed on the surface of TiO_2 NTs (Alver et al., 2020).

3.4. Photo-catalysis performance of TiO_2 NTs and TiO_2 NPs

3.4.1. Photo-catalysis kinetics of TiO_2 NTs and TiO_2 NPs

Adsorption and photo-catalysis of TiO_2 NTs are shown (Fig. 5a). Adsorption−desorption equilibrium was reached after 30 min in the dark. Subsequently, UV light was turned on to perform photo-catalysis experiments. Although TiO_2 NTs adsorbed 60.52% of MB, they exhibited high photo-catalytic activity, which indicates that self-assembled TiO_2 NTs contain photo-catalytic−active sites; moreover, these sites contribute to the generation of electron−hole pairs and radicals. TiO_2 NPs and TiO_2 NTs could completely remove MB in a short time, which especially demonstrates that TiO_2 NTs possess excellent removal capacity. Compared with TiO_2 NPs, TiO_2 NTs could catalytically degrade MB after the adsorption of MB, which achieves adsorption−photo-catalysis synergistic degradation of an organic pollutant. To further comprehend the diversity of TiO_2 NTs and TiO_2 NPs in terms of photocatalytic activity, rates of photo-catalysis after adsorption−desorption equilibrium were ascertained (Fig. 5b). Photo-catalytic process conformed to pseudo-first-order reaction kinetics (Equation (3)).

$$-\ln(C/C_0) = k_t + b \tag{3}$$

where: k_t is the rate constant of photo-catalysis (min^{-1}), C and C_0 are the concentrations of MB at time t and t_0 ($mg \cdot L^{-1}$), respectively, b is a constant.

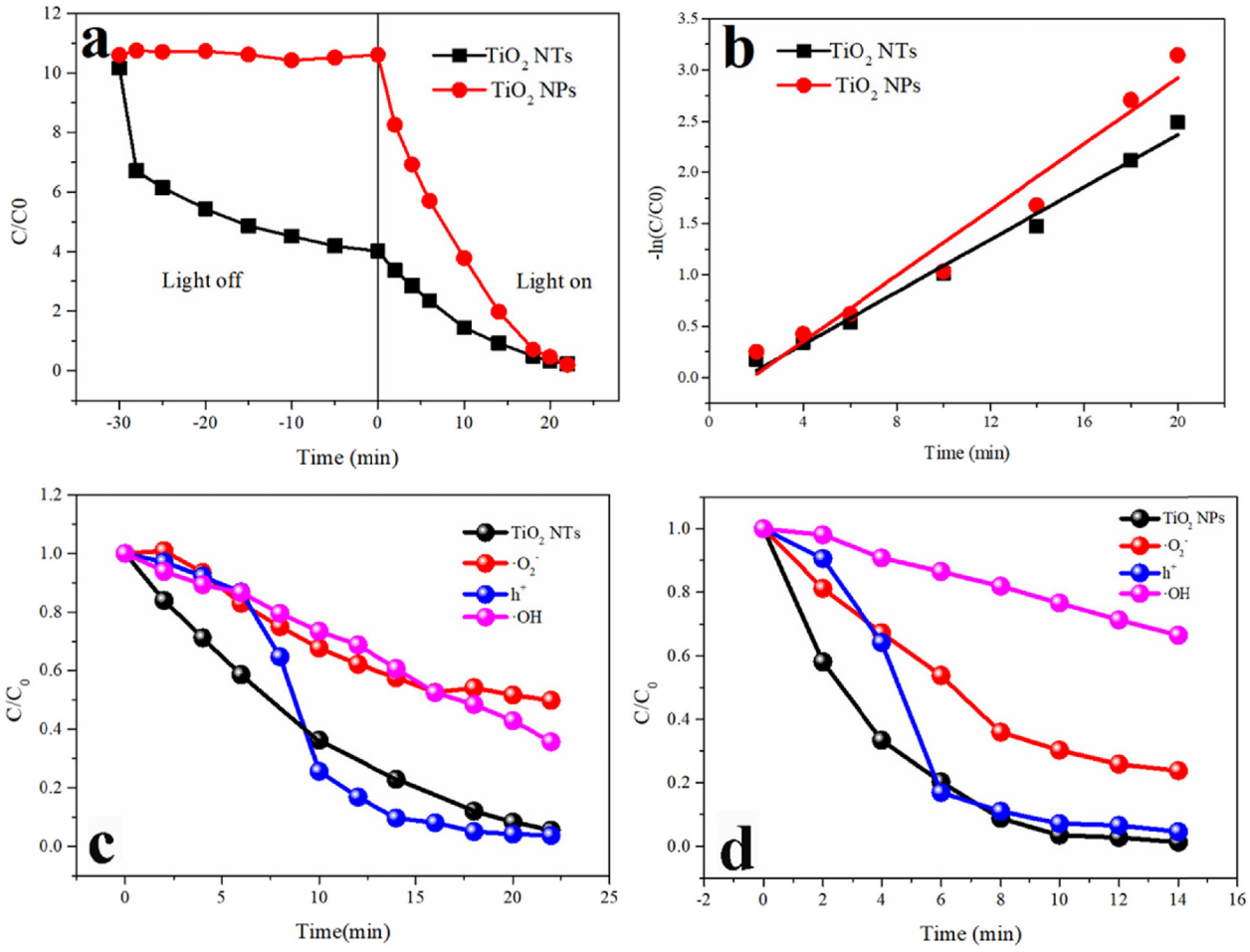

Fig. 5. Photo-catalytic degradation of MB by TiO_2 NTs and TiO_2 NPs (a) and linear simulation -ln (C/C_0) = kt of the kinetic curves for MB degradation (b); Free radical scavenging experiments of TiO_2 NTs(c) and TiO_2 NPs(d).

Rates of photo-catalysis of MB by use of TiO_2 NTs and TiO_2 NPs were 0.1277 and 0.1603 min^{-1}, which were calculated in Fig. 4b. Nevertheless, it is undeniable that TiO_2 NTs possesses excellent catalytic performance in terms of MB catalysis and present remarkable absorption–photo-catalysis synergy.

Stabilities of TiO_2 NPs and TiO_2 NTs before and after catalytic degradation of MB were assessed through TEM, XPS, and FTIR spectroscopy. When TiO_2 NTs and TiO_2 NPs catalyze MB, it can be noticed that they maintain their original appearance without any change, which suggests that TiO_2 NTs and TiO_2 NPs have good stability during catalytic degradation of MB (Fig. 2f and h). The structural stabilities of TiO_2 NPs and TiO_2 NTs after MB catalysis were determined by XPS and FTIR (Fig. 2j-k and Fig. 3a). The elements and functional groups are in agreement with that of original TiO_2 NPs and TiO_2 NTs and do not exhibit any changes. This result indicates that TiO_2 NPs and TiO_2 NTs possess excellent stability under UV light.

3.4.2. Mechanisms of photo-catalysis of MB by TiO_2 NTs and TiO_2 NPs

TiO_2 NTs not only have high adsorption capacity because of their mesoporous structures, but also have high catalytic activity (Fig. 5a-b). To explore mechanisms of photo-catalytic by TiO_2 NTs and TiO_2 NPs, effects of hydroxyl radicals ($\cdot OH$), superoxide radicals ($\cdot O_2^-$) and holes (h^+) on their catalytic behavior were determined (Fig. 5c-d). Efficiency of removal by TiO_2 NTs in the presence of various free radical scavengers is shown (Fig. 5c).

Compared with the efficiency of removal of MB in the absence of scavengers, removal of MB with holes (h^+) scavenger is first inhibited in early stages of photo-catalysis process and is not changed thereafter, which signifies that h^+ play an important role in the first stage of the photo-catalytic process. Furthermore, with addition of hydroxyl radical ($\cdot OH$) and superoxide radical ($\cdot O_2^-$) scavengers, the removal efficiency decreases to 64.28% and 50.12%, respectively, which indicates that $\cdot OH$ radicals and $\cdot O_2^-$ radicals are the main radicals in photocatalysis. It can be seen from Fig. 4d that the difference between TiO_2 NTs and TiO_2 NPs is that when TiO_2 NPs degrade MB, the dominating free radicals are $\cdot OH$ radicals, followed by $\cdot O_2^-$ radicals.

To further understand the conduction band (CB) energies of TiO_2 NTs and TiO_2 NPs, band gap energies of TiO_2 NTs and TiO_2 NPs were determined from the UV–visible diffuse reflectance spectrum (DRS) (Fig. 6). The absorption peak of TiO_2 NTs was approximately in the wavelength range of 200–500 nm TiO_2 NTs and TiO_2 NPs have strong absorption in the ultraviolet region (Fig. 6a). The band gap of TiO_2 NTs was calculated through the Tauc plot, which was obtained (Equation (4)).

$$(\alpha hv)^{1/n} = A(hv - Eg) \quad (4)$$

where α is the absorption coefficient, h is the Planck's constant ($6.63 \times 10-34$ J s), A is a constant, v is frequency (calculated by c/λ), c is light velocity (3×108 m s^{-1}), λ is wavelength (nm), Eg is semiconductor band gap, and n is index (which depends on the type of a semiconductor; when n = 2 or 1/2, a semiconductor is direct bandgap semiconductor or indirect bandgap semiconductor, respectively).

It is worth noting that α can be replaced by absorbance because they are proportional. A plot with $(\alpha hv)^{1/n}$ as the ordinate and hv as the abscissa was created. In addition, the straight part in the plot was extended to intersect the abscissa. The resultant intersection point was the band gap. The band gaps of TiO_2 NTs and TiO_2 NPs corresponded to 3.76 and 3.30 eV, respectively (Fig. 6b). The valence band (VB) energies (E_{VB}) of TiO_2 NTs and TiO_2 NPs were 2.79 and 2.61 eV, respectively, which were calculated by VB XPS (Fig. 6c). CB energy (E_{CB}) was calculated using the $E_{CB} = E_{VB}$ - Eg formula; therefore, the E_{CB} of TiO_2 NTs and TiO_2 NPs were −0.97 and −0.67eV, respectively.

The mechanism of the photo-catalytic degradation of MB by TiO_2 NTs or TiO_2 NPs is shown (Fig. 7). It was considered that photo-electron–hole pairs were generated under ultraviolet light while reduced photoelectrons (e^-) migrated from the VB to the CB, leaving oxidized h^+ in the VB. According to free radical scavenging experiments, h^+ cannot react directly with MB. The CB potential and the VB potential of TiO_2 NTs were more negative than the reduction potential of $E_0(O_2/\cdot O_2^-)$ and more positive than the potential of E_0 ($\cdot OH/H_2O$); therefore, the electrons could react with O_2 to produce $\cdot O_2^-$ and the holes could react with H_2O to generate $\cdot OH$. Ultimately, the $\cdot O_2^-$ and $\cdot OH$ mineralized MB into small molecules such as CO_2 and H_2O. The mechanism of MB degradation by TiO_2 NPs is similar to that of MB degradation by TiO_2 NTs. The difference is that $\cdot OH$ catalytic degradation of MB is the primary step, and $\cdot O_2^-$ catalytic degradation of MB is the secondary step. Consequently, compared with TiO_2 NPs, the decrease in the photocatalytic activity of TiO_2 NTs might be because of the increase in band gap, which reduces the absorbable range of light.

Electron–hole recombination rate is another important factor affecting the photo-catalytic activity of TiO_2 NTs and TiO_2 NPs. The PL spectra of TiO_2 NTs and TiO_2 NPs were collected in the wavelength range of 450–650 nm (Fig. 8a). The greater the intensity, the less the efficiency of recombination of the photo-generated carriers and thus longer the lifetime of photo-generated electron and holes pairs. As can be seen in Fig. 8a, intensity of TiO_2 NTs was slightly less than that of TiO_2 NPs, which indicates the electron–hole pairs of TiO_2 NTs are easier to recombine than those of TiO_2 NPs, which is one of the reasons why the catalytic activity of TiO_2 NTs is slightly less than that of TiO_2 NPs.

To evaluate photo-chemical properties of TiO_2 NTs and TiO_2 NPs, photo-current responses were measured (Fig. 8b). Electron–holes were generated by UV light irradiation; subsequently, the

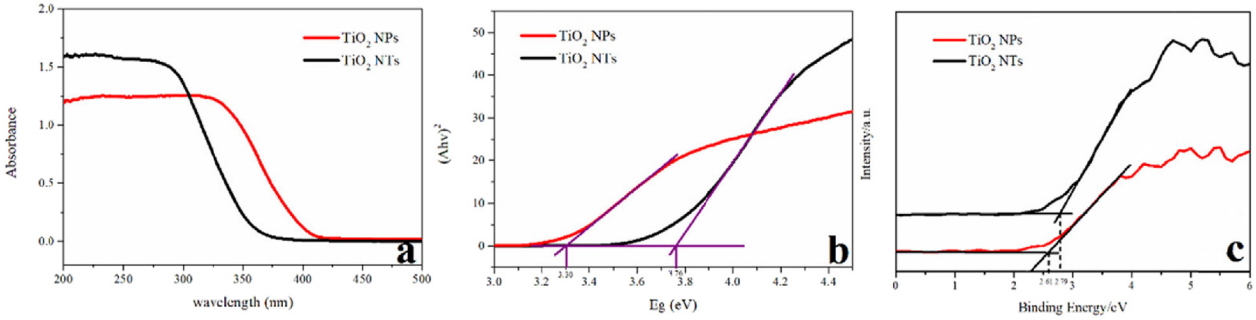

Fig. 6. UV–vis diffuse reflectance spectra (a), band gap energy (b), and Valence band X-ray photoelectron spectroscopy (c) of TiO_2 NTs and TiO_2 NPs.

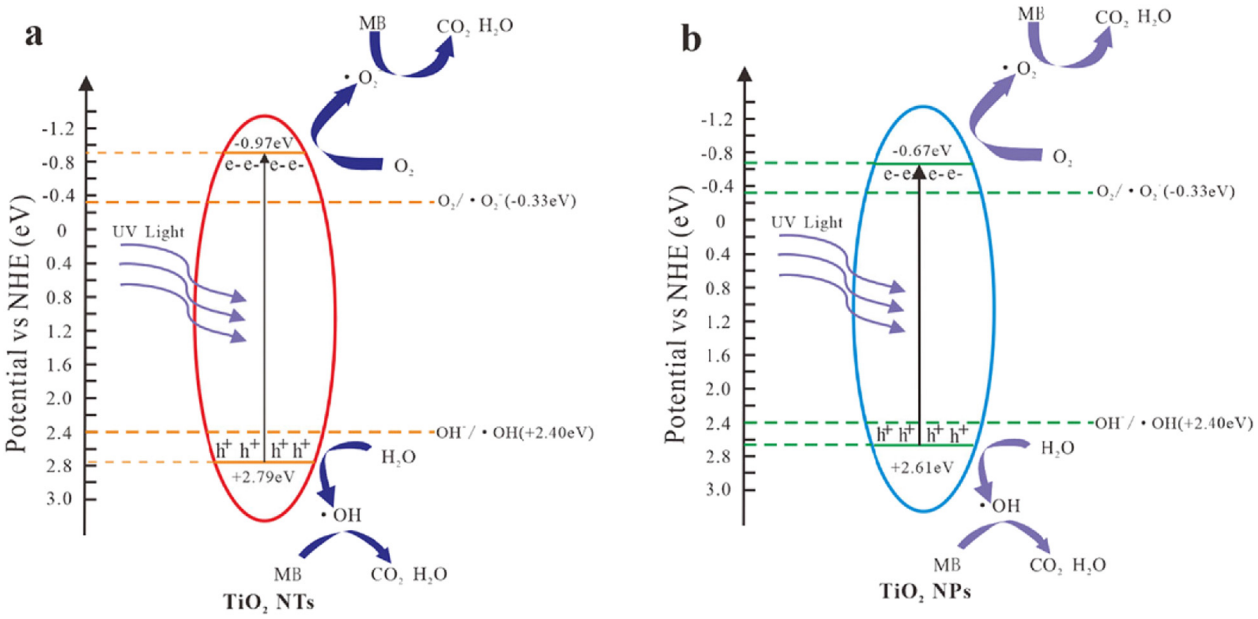

Fig. 7. Mechanism of TiO_2 NTs (a) and TiO_2 NPs (b) in photocatalytic degradation of MB.

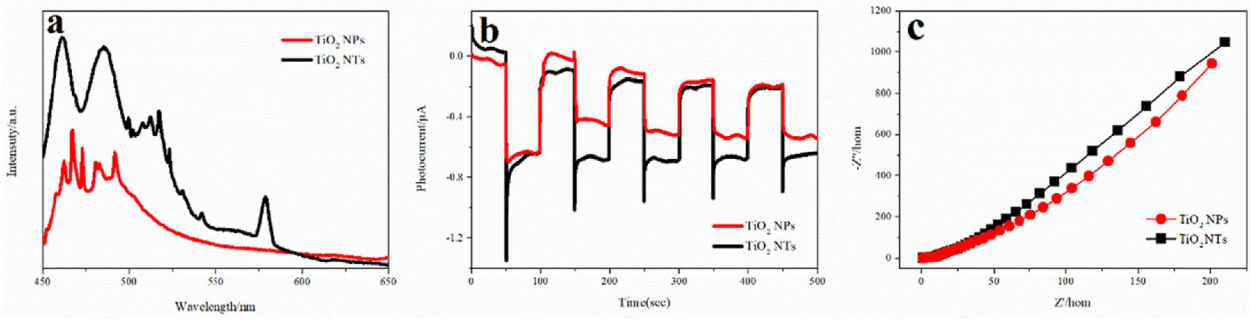

Fig. 8. Photoluminescence (PL) spectra (a), transient photocurrent responses of plots (b) and EIS Nyquist (c) of TiO_2 NTs and TiO_2 NPs.

photocurrent was measured using an electro-chemical station (Lv et al., 2019). The photo-current of TiO_2 NTs was weaker than that of TiO_2 NPs, which suggests that TiO_2 NPs have greater electron–hole separation efficiency and slower rates of recombination. EIS was conducted to determine the transfer rate of the electron–hole pairs. Arc radii Nyquist plots of TiO_2 NTs and TiO_2 NPs, show the separation efficiency of electron–hole pairs (Fig. 8c). The radius of the arc radii of TiO_2 NPs is significantly smaller than that of TiO_2 NTs, which indicates lesser interface between the electrolyte and photo-catalysts resistance and charge transfer resistance on the surface. Hence, the faster rates of migration of electron–hole pairs and slower recombination for TiO_2 NPs are than that of TiO_2 NTs, which results in relatively more radicals being generated that can degrade the pollutant and thus resulting in relatively greater photocatalytic activity.

4. Conclusions

In summary, titanate nanotubes with uniform hollow tubular structure were synthesized that possessed adsorption and photo-catalysis synergy concerning MB. TiO_2 NTs with sodium hexatite phase exhibited good MB adsorption because of its mesoporous structure, low isoelectric point and cation exchange mechanism. Conversely, TiO_2 NPs exhibited lesser MB adsorption. The high photo-catalytic activity of TiO_2 NPs resulted from the presence of anatase. The reduction in photo-catalytic activity of TiO_2 NTs was attributed to the easier recombination of photo-electron-hole pairs compared with that for TiO_2 NPs and the wider band gap energy than that of TiO_2 NPs. TiO_2 NTs exhibited excellent adsorption-photo-catalysis synergistic degradation of MB compared with other catalysts, which led to a degradation rate of 99% in a short time. When TiO_2 was transformed from nanoparticles to nanotubes, TiO_2 not only retained high photo-catalytic activity but also exhibited a significant increase in adsorption capacity. On the one hand, this study shows that the changes in structure and morphology would lead to a wide range of properties and possibly provide some research ideas for the study of adsorption-photo-catalysis bifunctional material synthesis. In contrast, the dual functions for removing pollutants in the water environment may be the focus of future research.

CRediT authorship contribution statement

Lin Niu: Investigation, Writing – original draft, Methodology. **Xiaoli Zhao:** Conceptualization, Methodology. **Zhi Tang:** Formal analysis, Data curation. **Hongzhou Lv:** Resources, Formal analysis. **Fengchang Wu:** Supervision, Resources. **Xiaolei Wang:** Visualization, Investigation. **Tianhui Zhao:** Data curation, Conceptualization.

Junyu Wang: Project administration, Supervision. **Aiming Wu:** Validation, Project administration. **John.P. Giesy:** Writing – review & editing.

Declaration of competing interest

The authors declare that they have no known competing financial interests or personal relationships that could have appeared to influence the work reported in this paper.

Acknowledgments

This work was supported by the National Science Fund for Distinguished Young Scholars [grant number 41925031] and the National Natural Science Foundation of China [grant number 41991315]. Dr. Giesy was supported through the Canada Research Chairs (CRC) program.

Appendix A. Supplementary data

Supplementary data to this article can be found online at https://doi.org/10.1016/j.jclepro.2021.126498.

References

Adeleke, J.T., Theivasanthi, T., Thiruppathi, M., et al., 2018. Photocatalytic degradation of methylene blue by ZnO/NiFe2O4 nanoparticles. Appl. Surf. Sci. 455, 195–200.
Ahmed, M.A., El-Katori, E.E., Gharni, Z.H., 2013. Photocatalytic degradation of methylene blue dye using Fe2O3/TiO2 nanoparticles prepared by sol–gel method. J. Alloys Compd. 553, 19–29.
Ahmed, M.A., Abou-Gamra, Z.M., Salem, A.M., 2017. Photocatalytic degradation of methylene blue dye over novel spherical mesoporous Cr 2 O 3/TiO 2 nanoparticles prepared by sol-gel using octadecylamine template. J. Environ. Chem. Eng. 5 (5), 4251–4261.
Al-Hajji, L.A., Ismail, A.A., Al-Hazza, A., et al., 2020. Impact of calcination of hydrothermally synthesized TiO2 nanowires on their photocatalytic efficiency. J. Mol. Struct. 1200.
Alver, E., Metin, A.U., Brouers, F., 2020. Methylene blue adsorption on magnetic alginate/rice husk bio-composite. Int. J. Biol. Macromol. 154, 104–113.
Alves, S.A., Patel, S.B., Sukotjo, C., et al., 2017. Synthesis of calcium-phosphorous doped TiO2 nanotubes by anodization and reverse polarization: a promising strategy for an efficient biofunctional implant surface. Appl. Surf. Sci. 399, 682–701.
Bian, Z., Feng, Y., Li, H., et al., 2021. Adsorption-photocatalytic degradation and kinetic of sodium isobutyl xanthate using the nitrogen and cerium co-doping TiO2-coated activated carbon. Chemosphere 263, 128254.
By Tomoko Kasuga, M.H., Hoson, Akihiko, Sekino, Toru, Niihara, Koichi, 1999. Titania nanotubes prepared by chemical processing. Adv. Mater. 11, 1307–1311.
Chen, Y., Zhang, X., Wang, L., et al., 2020a. Rapid removal of phenol/antibiotics in water by Fe-(8-hydroxyquinoline-7-carboxylic)/TiO2 flower composite: adsorption combined with photocatalysis. Chem. Eng. J. 402.
Chen, M., Wang, N., Zhu, L., 2020b. Single-atom dispersed Co-N-C: a novel adsorption-catalysis bifunctional material for rapid removing bisphenol A. Catal. Today 348, 187–193.
Chem. Eng. J., 2020 400.
Cheng, K., Cai, Z., Fu, J., et al., 2019. Synergistic adsorption of Cu(II) and photocatalytic degradation of phenanthrene by a jaboticaba-like TiO2/titanate nanotube composite: an experimental and theoretical study. Chem. Eng. J. 358, 1155–1165.
El-Yazeed, W.S.A., Ahmed, A.I., 2019. Photocatalytic activity of mesoporous WO3/TiO2 nanocomposites for the photodegradation of methylene blue. Inorg. Chem. Commun. 105, 102–111.
Fang, Z., Hu, Y., Cheng, J., et al., 2019. Continuous removal of trace bisphenol A from water by high efficacy TiO2 nanotube pillared graphene-based macrostructures in a photocatalytically fluidized bed. Chem. Eng. J. 372, 581–589.
Gao, N., Zhou, Y., Fan, M., et al., 2020. Promoting effect and role of alkaline earth metal added to ZrO2-TiO2-supported CeO2 for dichloromethane oxidation. Chem. Eng. J. 396.
Gu, Y., Yperman, J., Carleer, R., et al., 2019. Adsorption and photocatalytic removal of Ibuprofen by activated carbon impregnated with TiO2 by UV-Vis monitoring. Chemosphere 217, 724–731.
Guo, W., Zou, J., Guo, B., et al., 2020. Pd nanoclusters/TiO2(B) nanosheets with surface defects toward rapid photocatalytic dehalogenation of polyhalogenated biphenyls under visible light. Appl. Catal. B Environ. 277.
He, S., Yang, Z., Cui, X., et al., 2020. Fabrication of the novel Ag-doped SnS2@InVO4 composite with high adsorption-photocatalysis for the removal of uranium (VI). Chemosphere 260, 127548.
Hou, X., Jiang, S., Li, Y., 2019. A two-anode reduction technique to monitor the defect and dope the surface of TiO2 nanotube array as photo-anode for water splitting. Appl. Catal. B Environ. 258.
Huang, Q., Hu, Y., Pei, Y., et al., 2019. In situ synthesis of TiO2@NH2-MIL-125 composites for use in combined adsorption and photocatalytic degradation of formaldehyde. Appl. Catal. B Environ. 259.
Ibukun, O., Evans, P.E., Dowben, P.A., et al., 2019. Titanium dioxide-molybdenum disulfide for photocatalytic degradation of methylene blue. Chem. Phys. 525.
Jiang, F., Zheng, S., An, L., et al., 2012. Effect of calcination temperature on the adsorption and photocatalytic activity of hydrothermally synthesized TiO2 nanotubes. Appl. Surf. Sci. 258 (18), 7188–7194.
Kadam, A.N., Salunkhe, T.T., Kim, H., et al., 2020. Biogenic synthesis of mesoporous N–S–C tri-doped TiO2 photocatalyst via ultrasonic-assisted derivatization of biotemplate from expired egg white protein. Appl. Surf. Sci. 518.
Keereeta, Y., Thongtem, S., Thongtem, T., 2015. Enhanced photocatalytic degradation of methylene blue by WO3/ZnWO4 composites synthesized by a combination of microwave-solvothermal method and incipient wetness procedure. Powder Technol. 284, 85–94.
Kumar, S., Ojha, A.K., Walkenfort, B., 2016. Cadmium oxide nanoparticles grown in situ on reduced graphene oxide for enhanced photocatalytic degradation of methylene blue dye under ultraviolet irradiation. J. Photochem. Photobiol., B 159, 111–119.
Kusiak-Nejman, E., Wanag, A., Kapica- Kozar, J., et al., 2019. Methylene blue decomposition on TiO2/reduced graphene oxide hybrid photocatalysts obtained by a two-step hydrothermal and calcination synthesis. Catal. Today 357, 630–647.
Li, Y.-S., Li, T.-T., Song, X.-F., et al., 2020. Enhanced adsorption-photocatalytic reduction removal for Cr (VI) based on functionalized TiO2 with hydrophilic monomers by pre-radiation induced grafting-ring opening method. Appl. Surf. Sci. 514.
Lin, B.-Z., Li, X.-L., Xu, B.-H., et al., 2012. Improved photocatalytic activity of anatase TiO2-pillared HTaWO6 for degradation of methylene blue. Microporous Mesoporous Mater. 155, 16–23.
Liu, M., Yin, W., Qian, F.-J., et al., 2020. A novel synthesis of porous TiO2 nanotubes and sequential application to dye contaminant removal and Cr(VI) visible light catalytic reduction. J. Environ. Chem. Eng. 8 (5).
Lv, H., Zhao, X., Niu, H., et al., 2019. Ball milling synthesis of covalent organic framework as a highly active photocatalyst for degradation of organic contaminants. J. Hazard Mater. 369, 494–502.
Mekasuwandumrong, O., Pawinrat, P., Praserthdam, P., et al., 2010. Effects of synthesis conditions and annealing post-treatment on the photocatalytic activities of ZnO nanoparticles in the degradation of methylene blue dye. Chem. Eng. J. 164 (1), 77–84.
Nguyen-Phan, T.-D., Shin, E.W., 2011. Morphological effect of TiO2 catalysts on photocatalytic degradation of methylene blue. J. Ind. Eng. Chem. 17 (3), 397–400.
Nithya, M., Sathya, U., Keerthi, 2019. Hydrothermal synthesis and characterization of samarium doped BiPO4 with enhanced photocatalytic activity under UV radiation. Optik 193.
Pang, Y.L., Abdullah, A.Z., 2012. Effect of low Fe3+ doping on characteristics, sonocatalytic activity and reusability of TiO2 nanotubes catalysts for removal of Rhodamine B from water. J. Hazard Mater. 235–236, 326–335.
Qin, J., Zhang, X., Yang, C., et al., 2017. ZnO microspheres-reduced graphene oxide nanocomposite for photocatalytic degradation of methylene blue dye. Appl. Surf. Sci. 392, 196–203.
Qiu, L., Li, H., Dai, F., et al., 2020. Adsorption and photocatalytic degradation of benzene compounds on acidic F-TiO2/SiO2 catalyst. Chemosphere 246, 125698.
Sadeghzadeh-Attar, A., 2018. Efficient photocatalytic degradation of methylene blue dye by SnO2 nanotubes synthesized at different calcination temperatures. Sol. Energy Mater. Sol. Cell. 183, 16–24.
Sandoval, A., Hernández-Ventura, C., Klimova, T.E., 2017. Titanate nanotubes for removal of methylene blue dye by combined adsorption and photocatalysis. Fuel 198, 22–30.
Santhi, K., Navaneethan, M., Harish, S., et al., 2020. Synthesis and characterization of TiO2 nanorods by hydrothermal method with different pH conditions and their photocatalytic activity. Appl. Surf. Sci. 500.
Seo, M.H., Na, K.H., Yang, W.H., et al., 2020. Characterization of a TiO(2)/multi-wall carbon nanotube core-shell nanocomposite synthesized by a hydrothermal method. J. Nanosci. Nanotechnol. 20 (6), 3582–3587.
Shao, Y., Cao, C., Chen, S., et al., 2015. Investigation of nitrogen doped and carbon species decorated TiO2 with enhanced visible light photocatalytic activity by using chitosan. Appl. Catal. B Environ. 179, 344–351.
Sheng, Y., Wei, Z., Miao, H., et al., 2019. Enhanced organic pollutant photodegradation via adsorption/photocatalysis synergy using a 3D g-C3N4/TiO2 free-separation photocatalyst. Chem. Eng. J. 370, 287–294.
Shi, H., Zhang, T., Wang, H., 2011. Preparation and photocatalytic activity of La3+ and Eu3+ co-doped TiO2 nanoparticles: photo-assisted degradation of methylene blue. J. Rare Earths 29 (8), 746–752.
Sun, X., Li, Y., 2003. Synthesis and characterization of ion-exchangeable titanate nanotubes. Chemistry 9 (10), 2229–2238.
Tammina, S.K., Mandal, B.K., Kadiyala, N.K., 2018. Photocatalytic degradation of methylene blue dye by nonconventional synthesized SnO2 nanoparticles. Environ. Nanotechnol. Monitor. Manag. 10, 339–350.
Wan, X., Yuan, M., Tie, S-l, et al., 2013. Effects of catalyst characters on the

photocatalytic activity and process of NiO nanoparticles in the degradation of methylene blue. Appl. Surf. Sci. 277, 40–46.
Wang, D., Yu, B., Zhou, F., et al., 2009. Synthesis and characterization of anatase TiO2 nanotubes and their use in dye-sensitized solar cells. Mater. Chem. Phys. 113 (2–3), 602–606.
Wang, P., Zhou, Q., Xia, Y., et al., 2018. Understanding the charge separation and transfer in mesoporous carbonate-doped phase-junction TiO2 nanotubes for photocatalytic hydrogen production. Appl. Catal. B Environ. 225, 433–444.
Wang, H., Lu, J., Liu, L., et al., 2020. Ultra-thin rGO nanosheet modified TiO2 nanotube arrays for boosted photoelectrochemical performance. Appl. Surf. Sci. 506.
Wang G Q H, Y.Q., Duan, X.F., Sun, H.L., Xue, Q.K., 2002. Microstructure and formation mechanism of titanium dioxide nanotubes. Chem. Phys. Lett. 365, 427–431.
Ye, Z., Ye, Z., Nikiforov, A., et al., 2020. Influence of mixed-phase TiO2 on the activity of adsorption-plasma photocatalysis for total oxidation of toluene. Chem. Eng. J. 407, 126280.
Yu, J., Zou, J., Xu, P., et al., 2020. Three-dimensional photoelectrocatalytic degradation of the opaque dye acid fuchsin by Pr and Co co-doped TiO2 particle electrodes. J. Clean. Prod. 251.
Yu, Y., Wu, K., Xu, W., et al., 2021. Adsorption-photocatalysis synergistic removal of contaminants under antibiotic and Cr(VI) coexistence environment using nonmetal g-C3N4 based nanomaterial obtained by supramolecular self-assembly method. J. Hazard Mater. 404 (Pt A), 124171.
Zarghami, Z., Ramezani, M., Maddahfar, M., 2015. Simple microwave-assisted synthesis of Cu@CuSO4 as co-catalyst of TiO2 for photocatalytic degradation of methylene blue. Mater. Lett. 152, 21–24.
Zhang, X., Pan, J.H., Du, A.J., et al., 2009. Room-temperature fabrication of anatase TiO2 submicrospheres with nanothornlike shell for photocatalytic degradation of methylene blue. J. Photochem. Photobiol. Chem. 204 (2–3), 154–160.
Zhao, T., Tang, Z., Zhao, X., et al., 2019. Efficient removal of both antimonite (Sb(iii)) and antimonate (Sb(v)) from environmental water using titanate nanotubes and nanoparticles. Environ. Sci.: Nano 6 (3), 834–850.
Zheng, H., Meng, X., Chen, J., et al., 2021. In situ phase evolution of TiO2/Ti3C2T heterojunction for enhancing adsorption and photocatalytic degradation. Appl. Surf. Sci. 545.
Zhou, X., Zhou, S., Ma, F., et al., 2019. Synergistic effects and kinetics of rGO-modified TiO2 nanocomposite on adsorption and photocatalytic degradation of humic acid. J. Environ. Manag. 235, 293–302.
Zhu, L., Meng, Z-d, Cho, K-y, et al., 2012. Synthesis of CdS/CNT-TiO2 with a high photocatalytic activity in photodegradation of methylene blue. N. Carbon Mater. 27 (3), 166–174.
Zhu, C., Xu, J., Song, S., et al., 2020. TiO2 quantum dots loaded sulfonated graphene aerogel for effective adsorption-photocatalysis of PFOA. Sci. Total Environ. 698, 134275.
Zulfiqar, M., Chowdhury, S., Samsudin, M.F.R., et al., 2020. Effect of organic solvents on the growth of TiO2 nanotubes: an insight into photocatalytic degradation and adsorption studies. J. Water Process Eng. 37.

Difference in performance and mechanism when TiO_2 nanoparticles are converted to nanotubes: Adsorption and photo-catalysis synergistic effect to methylene blue

Lin Niu[a], Xiaoli Zhao[a*], Zhi Tang[a], Hongzhou Lv[a], Fengchang Wu[a], Xiaolei Wang[a], Tianhui Zhao[a], Junyu Wang[a], Aiming Wu[a], John.P.Giesy[a,b]

[a] State Key Laboratory of Environmental Criteria and Risk Assessment, Chinese Research Academy of Environmental Sciences, Beijing 100012, China.

[b] Toxicology Centre, University of Saskatchewan, Saskatoon, Saskatchewan, Canada

[*]Corresponding author: Xiaoli Zhao

E-mail: zhaoxiaoli_zxl@126.com

Figure captions

Figure S1. The high-resolution TiO_2 NPs XPS spectrum of before and after adsorption MB.

Figure S2. The high-resolution TiO_2 NTs XPS spectrum of before and after adsorption MB.

Figure S3. Recycling runs of TiO_2 NTs

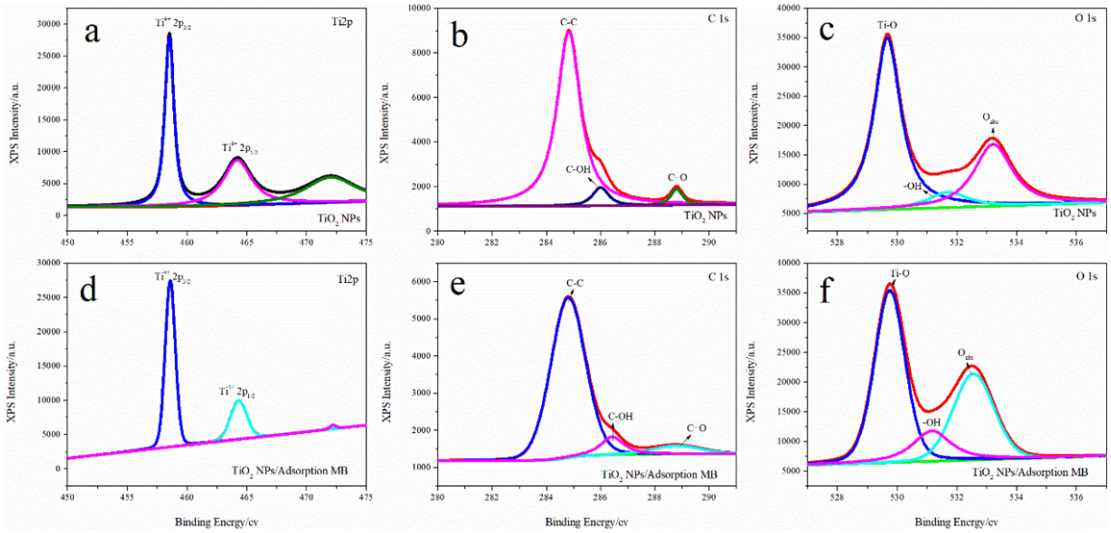

Figure. S1 The high-resolution TiO_2 NPs XPS spectrum of before and after adsorption MB.

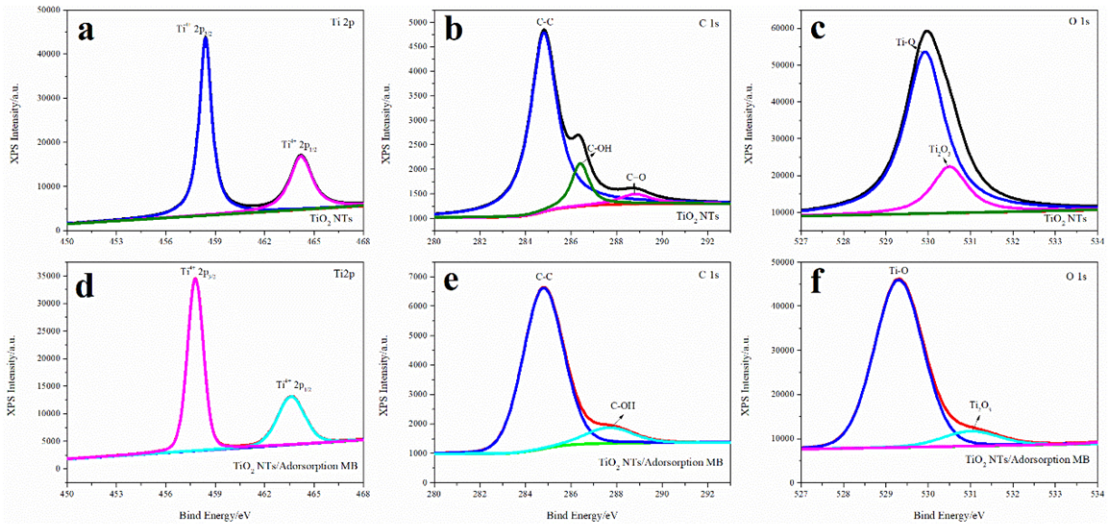

Figure. S2 The high-resolution TiO_2 NTs XPS spectrum of before and after adsorption MB.

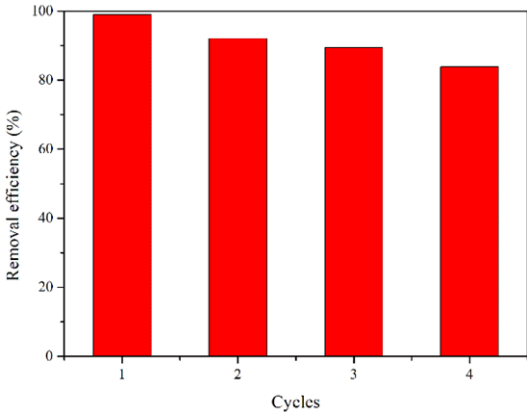

Figure. S3 Recycling runs of TiO_2 NTs